Surface Structures of Cubo-octahedral Pt-Mo Catalyst Nanoparticles from Monte Carlo Simulations

Guofeng Wang,[*]

Materials Sciences Division, Lawrence Berkeley National Laboratory, Berkeley, CA 94720

M.A. Van Hove,

Materials Sciences Division, Lawrence Berkeley National Laboratory, Berkeley, CA 94720;

Advanced Light Source, Lawrence Berkeley National Laboratory, Berkeley, CA 94720;

Department of Physics, University of California, Davis, CA 95616

P.N. Ross,

Materials Sciences Division, Lawrence Berkeley National Laboratory, Berkeley, CA 94720

M.I. Baskes

MST-8 Structure / Property Relations Group, Los Alamos National Laboratory, Los Alamos, NM 87545

RECEIVED DATE (to be automatically inserted after your manuscript is accepted if required according to the journal that you are submitting your paper to)

[*] Corresponding author. Email: gfwang@lbl.gov

Abstract - The surface structures of cubo-octahedral Pt-Mo nanoparticles have been investigated using the Monte Carlo method and modified embedded atom method potentials that we developed for Pt-Mo alloys. The cubo-octahedral Pt-Mo nanoparticles are constructed with disordered fcc configurations, with sizes from 2.5 to 5.0 nm, and with Pt concentrations from 60 to 90 at. %. The equilibrium Pt-Mo nanoparticle configurations were generated through Monte Carlo simulations allowing both atomic displacements and element exchanges at 600 K. We predict that the Pt atoms weakly segregate to the surfaces of such nanoparticles. The Pt concentrations in the surface are calculated to be 5 to 14 at. % higher than the Pt concentrations of the nanoparticles. Moreover, the Pt atoms preferentially segregate to the facet sites of the surface, while the Pt and Mo atoms tend to alternate along the edges and vertices of these nanoparticles. We found that decreasing the size or increasing the Pt concentration leads to higher Pt concentrations but fewer Pt-Mo pairs in the Pt-Mo nanoparticle surfaces.

Introduction

Fuel cells can transform chemical energy carried by hydrogen fuel into electrical energy with high efficiency and with no pollutant production. Therefore, it is of great significance to develop novel materials for fuel cells to achieve low cost, high performance and long durability. For low-temperature fuel cells, new electrode catalysts that have less precious metal such as Pt yet good performance are highly desirable. [1] Alloying Pt with a second lower-cost element can be used to fulfill this goal. [2-6] An essential step to designing Pt bimetallic catalysts is knowledge of the equilibrium concentration of Pt and the arrangement of the two metals in the surfaces of their bimetallic nanoparticles. However, it is still very difficult to characterize the details of bimetallic nanoparticle surfaces experimentally. Alternatively, atomistic simulations can provide much insight into the surface chemistry of multi-component nanoparticles. [7-9] In this work, we have investigated the segregation of Pt atoms and the arrangement of Pt and Mo atoms in the surfaces of equilibrium cubo-octahedral Pt-Mo nanoparticles, using the modified embedded atom method (MEAM) [10] and the Monte Carlo (MC) method.

Earlier, we have successfully applied MEAM potentials and the same MC method to modeling the segregation of Pt atoms to the surfaces of Pt-Re [11] and Pt-Ni [12] nanoparticles. Note that, while pure bulk Pt and Ni assumes the face-centered cubic (fcc) structure, pure bulk Re adopts the hexagonal closed-packed (hcp) structure, and pure bulk Mo has the body-centered cubic (bcc) crystal structure. In addition, Pt segregates to surfaces in different fashions in these three alloy systems. In Pt-Re alloys, Pt is predicted to strongly segregate to the surfaces. Hence, equilibrium Pt-Re nanoparticles will form a Pt-enriched shell and a Re-enriched core. [11] At close-packed crystal facets of Pt-Ni nanoparticles, Pt strongly segregates to the outermost and third layers, while Ni segregates to the second layer below the surface. As a result, equilibrium Pt-Ni nanoparticles assume a surface-sandwich structure. [12] Experimental results indicate that Pt will segregate to the Pt-Mo surfaces rather weakly. [13] Therefore, one aim of this series of investigations is to establish that the MEAM approach is capable of accurately simulating surface phenomena for a broad spectrum of Pt bimetallic alloys. Compared to the original embedded-atom method (EAM) that yields good results only for fcc metals, [14,15] the MEAM potentials include the effects of directional bonding and therefore are applicable also to bcc and hcp metals.

Furthermore, it has been found that the Pt-Mo alloy is a promising candidate for CO-tolerant anode catalysts of proton exchange membrane fuel cells (PEMFCs). [13, 16-19] Grgur *et al* [17] reported that the electro-oxidation of H_2 and H_2/CO mixtures on carbon supported Pt-Mo alloy catalysts depends on the composition of nanoparticle surfaces and that there exists an optimal composition for Pt-Mo alloy catalysts to yield best catalytic performance. These results are consistent with the idea of a "bi-functional mechanism": CO adsorbed on Pt could be only oxidized by a neighboring oxygen-containing surface species adsorbed on Mo. Density functional theory (DFT) calculations for $Pt_2Mo(111)$ surfaces confirmed that CO is absorbed weakly on both Pt and Mo sites (compared with Pt-Ru surfaces) and OH (the assumed oxygen-containing surface species) is only strongly adsorbed on Mo. [20] Hence, it is of practical use to simulate the equilibrium surface structures of Pt-Mo nanoparticles in order to further design and improve Pt-Mo alloy catalysts for fuel cells.

The Monte Carlo Method

Starting from some atomic configuration, a series of Pt-Mo nanoparticle configurations can be generated using the MC method. In the equilibrated stage of MC simulations, the probabilities of an equilibrium configuration occurring are proportional to the Boltzmann distribution of the equilibrium ensemble. At each MC step, one of the following two configuration changes is attempted with an equal probability:

(a) A randomly selected atom is displaced from its original position in an arbitrary direction. The magnitude of the displacement is in the range of $(0, r_{max}]$. At a given temperature, the maximum displacement r_{max} is chosen so that the acceptance rate of new configurations is about 0.5 during the equilibrated part of the simulations.

(b) Two randomly selected atoms with different element types exchange their positions.

If the configuration change leads to a decrease in energy, the new configuration is always retained. If the change increases the system energy, the new configuration is retained with a probability given by the Boltzmann factor for the energy change.

After repeating the above procedures for multi-million MC steps, physical quantities of interest (such as the Pt concentration profile) are obtained by averaging over the generated equilibrium configurations.

Modeling atomic interactions in Pt-Mo alloy systems

Developing the MEAM potentials for Pt-Mo alloys. In this work, we used the same first-nearest-neighbor (1NN) MEAM potential for pure Pt as that used in our previous studies. [11,12] However, we used a second-nearest-neighbor (2NN) MEAM potential [21,22] for bcc Mo. The original 1NN MEAM potential for Mo erroneously predicted that the high-density (110) surface would have a higher surface energy than the low-density (111) surface in bcc crystals. [10] The 2NN MEAM potential solved this problem by including the interactions between second nearest neighbors, whose distances are only about 15 % larger than the separations between the first nearest neighbors in bcc crystals. We chose Pt_3Mo with a $L1_2$ structure as the reference structure to evaluate the cross-interaction potentials between Pt and Mo. In this way, we can calculate the Pt-Mo pair potentials using the method presented before. [11, 23]

The parameters of MEAM potentials for fcc Pt and bcc Mo were fitted to reproduce empirical data, namely cohesive energy, lattice constant, elastic constants, and vacancy formation energy.[10, 22] The parameters of the MEAM cross potential between Pt and Mo were fitted to first-principles calculation results for Pt_3Mo ($L1_2$). To obtain these first-principles calculation results, we evaluated the system energies using density-functional theory in the local density approximation. We employed the PARATEC code [24,25] that performs quantum-mechanical total energy calculations using pseudopotentials and a plane-wave basis set. In this work, we used the package FHI98PP [26] to generate the norm-conserving Troullier-Martins [27] type of pseudopotentials, employing common parametrizations of the local-density approximation for exchange and correlation. In all calculations, we have used a 16x16x16 k-point grid for k-space integration and a kinetic energy cutoff of 60 Ry to expand the electronic wave functions in the plane wave basis.

The parameters for the Pt-Mo MEAM potentials are given in Table 1. Table 2 lists the angular screening parameters. Table 3 gives the properties for Pt_3Mo ($L1_2$) calculated using the MEAM and the first-principles methods. It is noticeable that the two calculations agree poorly for the elastic constants C_s and C_{44} of Pt_3Mo ($L1_2$); we found no improvement within the current MEAM formalism. This indicates some limitations present in the accuracy of the developed cross potentials for Pt and Mo. However, the elastic constants C_s and C_{44} are shear moduli which describe the material resistance to shear deformations. It is conceivable that the discrepancy in these shear elastic constants would have a minor influence on our results of the equilibrium surface structures of Pt-Mo alloys. As shown in the following, the current MEAM potentials for Pt-Mo alloys indeed predict a weak Pt segregation in extended surfaces, quantitatively agreeing with experimental measurements.

Testing the Pt-Mo MEAM potentials. An accurate simulation of segregation phenomena in alloy surfaces requires good theoretical predictions of surface energies for the component metals. In this respect, the MEAM potentials have yielded better results than the original EAM potentials. [10] We report in Table 4 the calculated low-indexed surface energies for pure bcc Mo and fcc Pt using the developed MEAM potentials. These results show a good agreement in surface energies among the MEAM

potentials, results from another first-principles study [28] and experimental results. [29,30] Moreover, the closed-packed surfaces, (110) in a bcc structure and (111) in an fcc structure, are correctly predicted to have the lowest surface energies using our MEAM potentials. In this work, we are only interested in Pt-rich Pt-Mo alloys, which assume fcc crystal structures. The MEAM potentials lead to a cohesive energy of fcc Mo that is 0.32 eV higher than bcc Mo. The calculated fcc-bcc energy difference is close to the experimental value of 0.28 eV. [31] We should have evaluated surface energies for pure Mo with an fcc lattice in Table 4, since we are interested in Pt-Mo alloys with fcc structures. However, both the MEAM potentials and first-principles calculations indicate that fcc Mo is unstable and will transform to lower energy structures under the volume-conserving tetragonal deformation. As a result, the energies for the relaxed low-index surfaces of fcc Mo are not attainable.

Furthermore, we tested our MEAM potentials by calculating the segregation profiles for (111) and (100) extended surfaces of fcc Pt-Mo alloys. It was found that the Pt-Mo solid solutions can contain as high as 42 at. % Mo and still maintain fcc crystal structures. [32] Therefore, we chose to investigate four bulk compositions of fcc Pt-Mo alloys: $Pt_{60}Mo_{40}$, $Pt_{70}Mo_{30}$, $Pt_{80}Mo_{20}$, and $Pt_{90}Mo_{10}$. To simulate extended surfaces, we used slab simulation cells in which periodic boundary conditions are only applied in the two directions parallel to the surface and with fixed cell dimensions in those directions. In these simulation cells, there are two equivalent extended surfaces on either side of the slab. In the initial configurations, the atomic separations were determined using the calculated lattice constants of the bulk alloys at the same simulation temperature and the same overall composition, and the Pt and Mo atoms were randomly distributed. There are 36 atoms for (111) and 32 atoms for (100) in each layer parallel to the surfaces of our simulation slabs. The thickness of the simulation slabs is about 30 Å. Starting from an initial surface configuration, each extended surface slab was equilibrated using Monte Carlo simulations allowing both positional and compositional relaxations at a temperature of 1000 K.

We performed the MC simulations up to 10×10^6 steps. To eliminate the influence of the initial configurations, we discarded the first 2×10^6 configurations in our analysis. The Pt concentrations in the surface layers and central region of the simulation slabs were evaluated by averaging the sample

configurations every 10^3 MC steps. Due to the finite thickness of our simulation cells, the surface segregation of Pt atoms leads to a lower concentration of Pt in the central region of the slabs. To be consistent with the lattice constants used in our simulations, we must do a series of MC simulations for each extended surface with different overall compositions and reestablish the desired bulk composition in the center of the slabs.

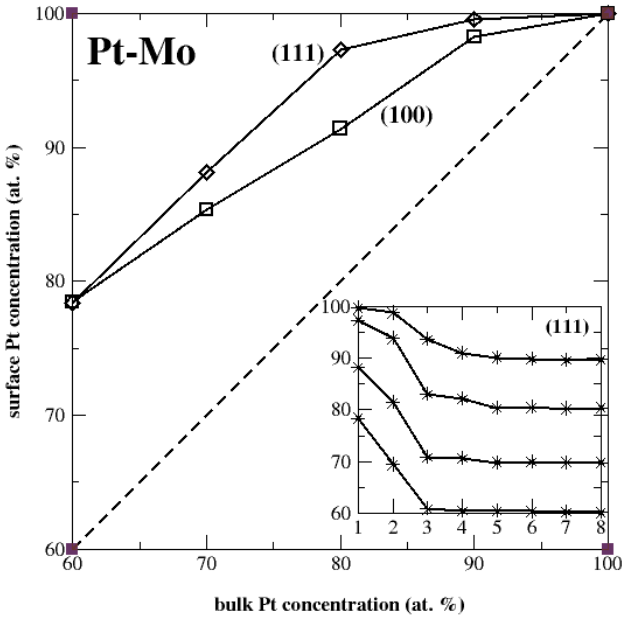

Figure 1. Calculated Pt concentrations in the outermost layer of (111) and (100) extended surfaces as a function of the bulk composition of Pt-Mo alloys. The temperature of the MC simulations is 1000 K. The diamonds stand for the results for (111) surfaces and the squares are the results for (100) surfaces. The dashed line indicates where the surface concentration equals the bulk value. Inset: calculated Pt concentration depth profiles for the (111) surface of Pt-Mo alloys at T=1000 K.

Figure 1 shows the calculated extent of Pt atom segregation to the Pt-Mo extended surfaces. Compared to the bulk compositions (dashed line), the Pt concentrations in the outermost layer of (111) and (100) surfaces (solid lines) are higher. In other words, the Pt atoms tend to segregate to the surfaces of Pt-Mo alloys. As shown in the inset of Fig. 1, the Pt concentration decreases monotonically and smoothly from the (111) surface to the bulk within four atomic layers. Our simulation results are consistent with a qualitative prediction using a simple tight-binding theory of surface segregation in transition metal alloys.[33] Grgur *et al.* measured a Pt concentration of 77 at. % in the outermost surface

layer of $Pt_{70}Mo_{30}$ poly-crystals annealed at 970 K.[13] We found the Pt concentrations to be 88 at. % and 85 at. % in the outermost layer of (111) and (100) surfaces of $Pt_{70}Mo_{30}$ alloys from MC simulations. The discrepancy between theory and experiment is only about 10 at. %. Grgur *et al.* pointed out in Ref. 13 that the short annealing time (30 min) in their study might lead to an underestimation of Pt segregation. Therefore, our Pt-Mo MEAM potentials are suitable for quantitatively predicting surface segregation of Pt atoms in Pt-Mo alloys.

Monte Carlo Simulations on Pt-Mo nanoparticles

The surface structures of bimetallic nanoparticles are affected by the shape, size, and composition of the nanoparticles. X-ray diffraction data indicate that the carbon-supported Pt-Mo nanoparticles have fcc lattices at least when the Pt concentration is higher than 75 at. %. [17,19] Hence, to model the Pt-Mo nanoparticles, we used the cubo-octahedral shape (shown in Fig. 2), which assumes the fcc lattice and is terminated by the low-energy {111} and {100} facets. The cubo-octahedron (or half cubo-octahedron) was found to be the equilibrium shape for other Pt bimetallic nanoparticles (such as Pt-Ni [4] and Pt-Ru [34]). For small nanoparticles, the surface/volume ratio and the average coordination number of surface atoms vary nonlinearly with their sizes. [35] For this reason, we simulated the Pt-Mo nanoparticles with four different sizes (listed in Table 5) in this work. These four sizes cover a range of particle diameter from about 2.5 to 5.0 nm and a range of surface/volume ratio from about 0.27 to 0.46. As with the study of extended surfaces, we also chose $Pt_{60}Mo_{40}$, $Pt_{70}Mo_{30}$, $Pt_{80}Mo_{20}$, and $Pt_{90}Mo_{10}$ as the compositions of Pt-Mo nanoparticles in our MC simulations.

The cubo-octahedral Pt-Mo nanoparticles were initially constructed with the lattice constants of the same-composition bulk alloys at T=600 K and with randomly distributed Pt and Mo atoms. For each nanoparticle, we performed MC simulations for 10×10^6 steps at T=600 K. During the MC simulations, both the atomic positions and the distribution of the metal atoms in the nanoparticles were allowed to change. As a result the shape and average interatomic distance of nanoparticles can also change. To quantitatively characterize the equilibrium Pt-Mo nanoparticles, we calculated the properties of interest by averaging the values sampled every 10^3 steps in the last 5×10^6 steps of the MC simulations.

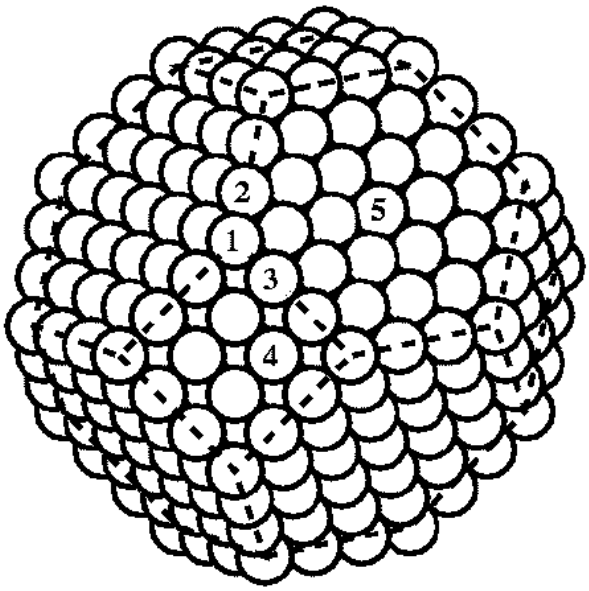

Figure 2. A fcc cubo-octahedral nanoparticle. The numbers label atoms at non-equivalent surface sites in the outermost layer of the particle. They have different numbers of nearest neighbors: atom 1: vertex (six nearest neighbors); atom 2: {111}/{111} edge (seven nearest neighbors); atom 3: {111}/{110} edge (seven nearest neighbors); atom 4: {100} facet (eight nearest neighbors); and atom 5: {111} facet (nine nearest neighbors).

Equilibrium structures. Using external and cross-sectional views, we show in Fig. 3 final snapshots of the $Pt_{60}Mo_{40}$, $Pt_{70}Mo_{30}$, and $Pt_{80}Mo_{20}$ nanoparticles from our MC simulations. Compared to the bulk-terminated cubo-octahedrons (shown in Fig. 2), the equilibrium Pt-Mo nanoparticles appear to be much rounder, as we also found with Pt-Ni and Pt-Re nanoparticles. [11,12] This is because, to lower the energy, the atoms at the low-coordination sites (edges and vertices) relax inward more than those at the facet sites. These plots qualitatively show that Pt atoms are enriched in the surface of the nanoparticles. Moreover, the Mo atoms preferentially occupy the low-coordination edge and vertex sites at the surface. These features are seen most prominently in Fig. 3(c) for the $Pt_{80}Mo_{20}$ nanoparticle: the facets are fully occupied by Pt atoms, the Mo atoms only appear at the edges and vertices, and the Pt and Mo atoms arrange themselves in an alternating sequence to achieve a maximal number of Pt-Mo pairs along the edges and vertices.

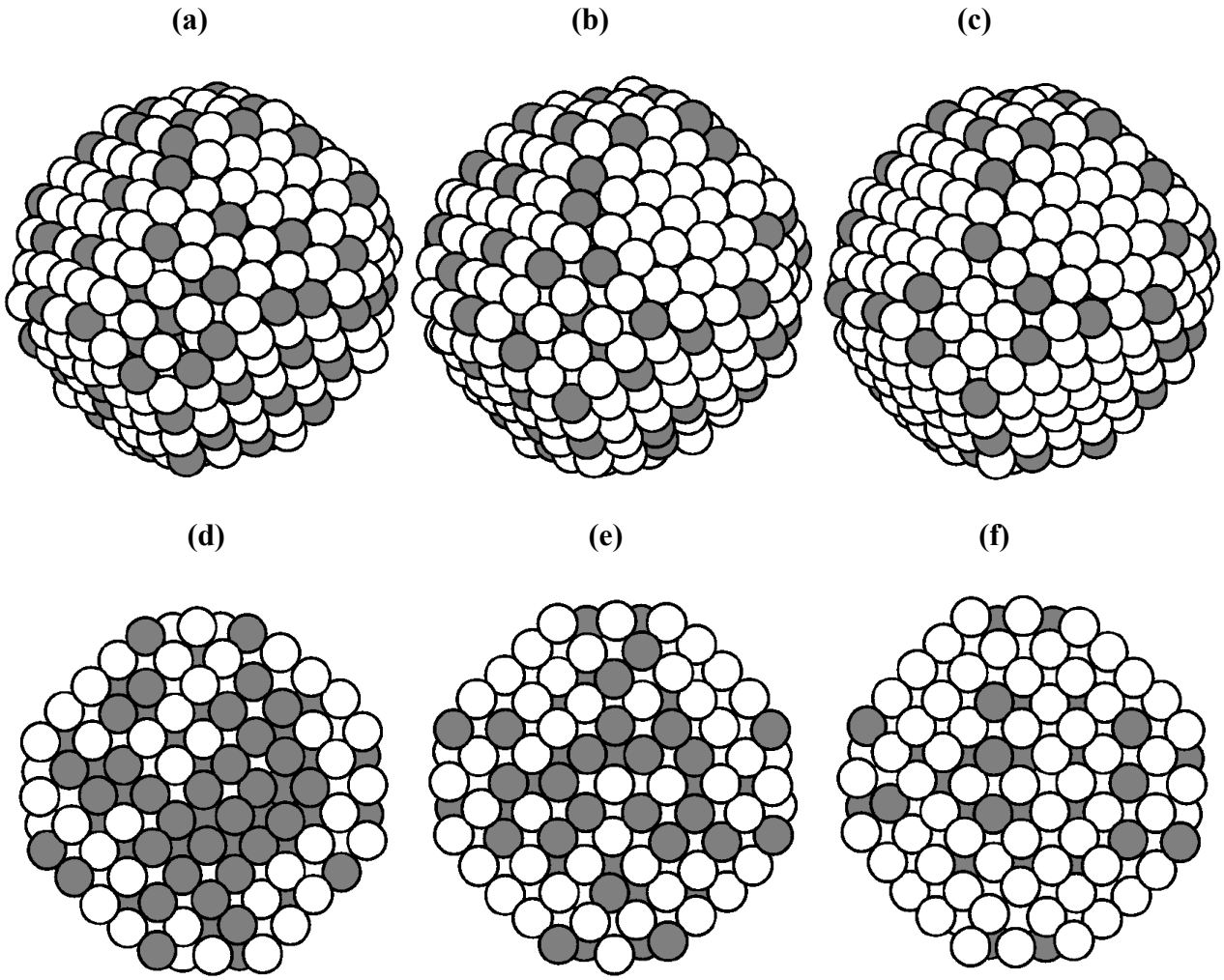

Figure 3. Snapshots of equilibrium cubo-octohedral Pt-Mo nanoparticles (containing 586 atoms) simulated at T=600 K. (a), (b), and (c) show external views of typical $Pt_{60}Mo_{40}$, $Pt_{70}Mo_{30}$, and $Pt_{80}Mo_{20}$ nanoparticles, respectively. (d), (e), and (f) show [001] cross-sectional views of the same nanoparticles, respectively. In these snapshots, the open circles represent the Pt atoms and the gray circles stand for the Mo atoms.

Distinct from the nanoparticles with other compositions, the $Pt_{90}Mo_{10}$ nanoparticle shown in Fig. 4(a) exhibits a single reconstructed {100} facet. It is well known that the outermost layer of the (100) surface of pure elemental Pt undergoes a reconstruction from a square to a hexagonal lattice, while the (111) surface does not reconstruct, remaining hexagonal. [36,37] Since the relaxed $Pt_{90}Mo_{10}$ nanoparticle has a nearly pure Pt outermost layer, one may expect to observe this transformation from the original square to a hexagonal arrangement of atoms in {100} facets in our MC simulations. We have in fact

found the same {100}-facet reconstruction process in our previous simulations for Pt-Re [11] and Pt-Ni [12] cubo-octahedral nanoparticles. However, unlike in Pt-Re and Pt-Ni nanoparticles where all {100} facets reconstruct, we find that only one {100} facet reconstructs in the $Pt_{90}Mo_{10}$ nanoparticle containing 586 atoms in the single Monte Carlo simulation that we ran for this nanoparticle. Figure 4(b) shows an unreconstructed {100} facet that keeps its square lattice after many MC simulation steps in the same nanoparticle. Comparing Fig. 4(a) and (b), we notice that there are a few Mo atoms in the edges surrounding the unreconstructed {100} facet in Fig. 4(b), but there are no Mo atoms around the reconstructed {100} facet in Fig. 4(a). It appears that Mo atoms in {100} facets prevent the reconstruction from happening. This explains why we find no reconstructed {100} facets in the $Pt_{60}Mo_{40}$, $Pt_{70}Mo_{30}$, and $Pt_{80}Mo_{20}$ nanoparticles: there are always some Mo atoms in the edges of {100} facets of those nanoparticles (see Fig. 3). It should be noted that fewer or more than one {100} facet could reconstruct in $Pt_{90}Mo_{10}$ nanoparticles, depending on the existence or absence of Mo atoms in the {100} facets.

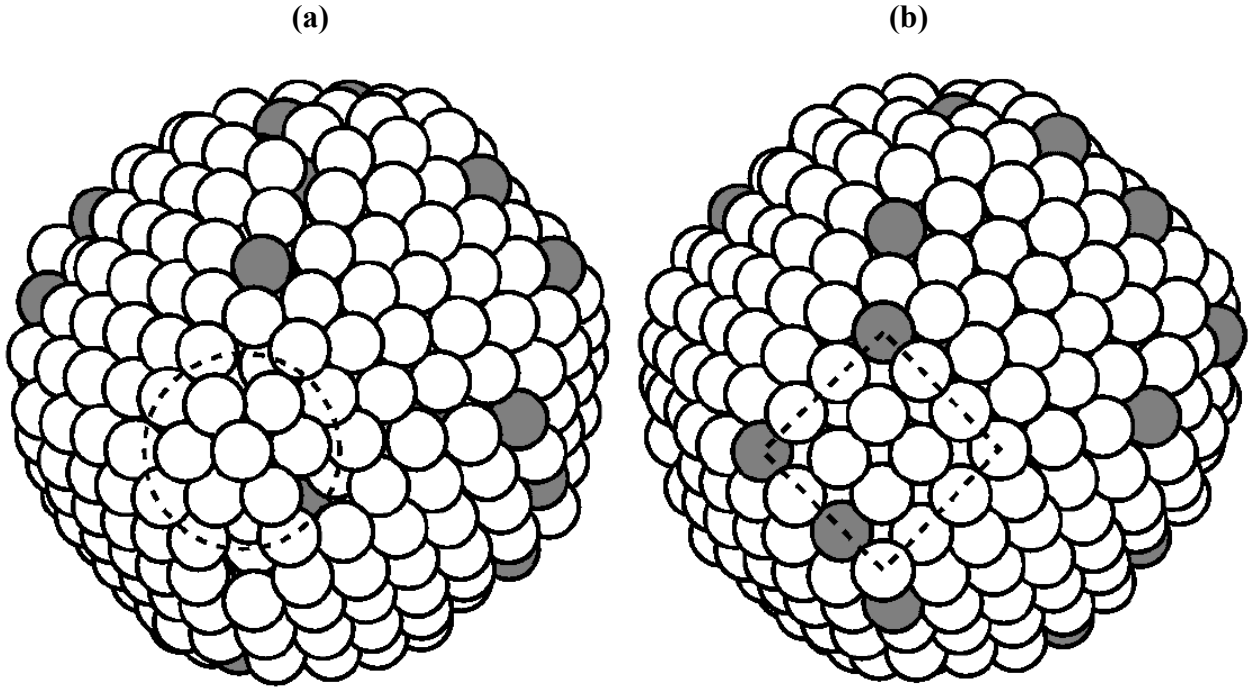

Figure 4. An equilibrium configuration of a cubo-octohedral $Pt_{90}Mo_{10}$ nanoparticle (containing 586 atoms) after 10×10^6 MC simulation steps at T=600 K, viewed from two different directions. The two panels show two different {100} facets: (a) a reconstructed {100} facet and (b) an unreconstructed

{100} facet. As a guide to the eye, the edges of the two {100} facets are indicated with dashed lines. In these snapshots, the open circles represent the Pt atoms and the gray circles stand for the Mo atoms.

Both DFT calculations [20] and experiments [13,17] imply that the existence of Mo atoms in the surface is the major reason for Pt-Mo catalysts to have a good tolerance toward CO. Since there are too few Mo atoms in the surface, the $Pt_{90}Mo_{10}$ nanoparticles are not considered as good catalysts for their application in fuel cells. In addition, we found that both Pt-Re [11] and Pt-Ni [12] nanoparticles can achieve a pure Pt skin structure at a lower Pt concentration than $Pt_{90}Mo_{10}$ nanoparticles. Thus, Pt-Re and Pt-Ni nanoparticles are better candidates if an economical Pt bimetallic catalyst is needed. Therefore, from here on in this work, we only consider equilibrium Pt-Mo nanoparticles with the three other compositions.

Segregation of Pt atoms. Figures 3 and 4 show qualitatively that the Pt atoms are enriched in the surfaces of Pt-Mo nanoparticles. In particular, an almost pure Pt skin is formed in the surface of $Pt_{90}Mo_{10}$ nanoparticles. In Fig. 5, we plot the calculated Pt concentration in the outermost layer of Pt-Mo nanoparticles. We observe the following two trends from these quantitative results. First, the Pt concentration in the surfaces are 5 to 14 at. % higher than the overall Pt concentration in the nanoparticles. This enrichment is consistent with our MC simulation results shown in Fig.1 for the low-index surfaces of Pt-Mo alloys. Second, the extent of Pt segregation to the surfaces increases with nanoparticle size. The surface Pt concentrations of the nanoparticles containing 586 atoms are about 6 at.% lower than those of the Pt-Mo nanoparticles containing 4033 atoms.

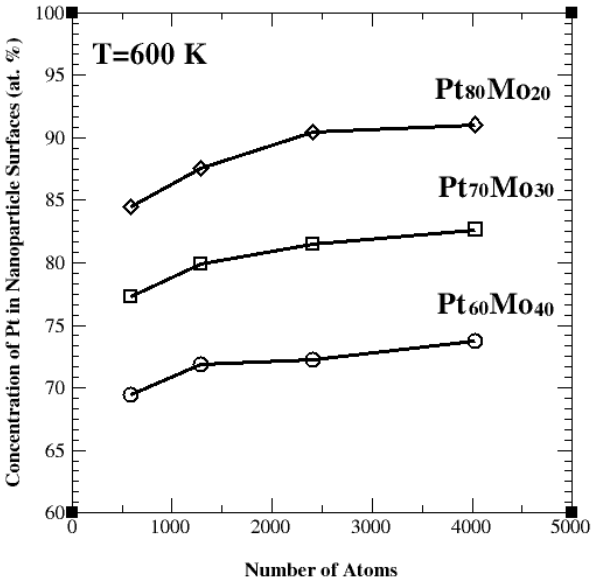

Figure 5. Calculated Pt concentrations in the nanoparticle surface as a function of the number of atoms in Pt-Mo nanoparticles at T=600 K.

To understand the size effect on Pt segregation in these nanoparticles, we further calculated the Pt concentrations at various surface sites distinguished by their number and arrangement of first nearest neighbors (see the caption of Fig. 2). In Fig. 6, we divide the surface atoms of nanoparticles into three groups: {111} facets, {100} facets, and low-coordination sites (including edges and vertices). Figure 6 shows that the Pt atoms do not distribute themselves homogeneously in the nanoparticle surfaces. Instead, the Pt atoms preferentially segregate to the high-coordination surface sites, namely within the {111} and {100} facets. In most simulated Pt-Mo nanoparticles, the Pt concentrations at {111} facet sites (having nine nearest neighbors) are also higher than those at {100} facet sites (having eight nearest neighbors). Since the larger nanoparticles have a higher ratio of {111} and {100} facet sites vs. edge and vertex sites (see Table 5), the preferential segregation of Pt atoms to the facet sites causes a higher Pt concentration in the surface of large nanoparticles than small ones.

Comparing the results of Pt-Mo nanoparticles with three different compositions in Fig. 6, we find that increasing the overall Pt concentration in nanoparticles leads to nearly the same increase in the Pt concentration at the {111} and {100} facets. However, the Pt concentration at the low-coordination surface sites stays around 60 at. %, fairly insensitive to the change of nanoparticle composition. It

appears that the Pt and Mo atoms tend to form pairs, alternating along the edges and vertices regardless of the composition. The edge and vertex atoms have higher potential energies, so these atoms are considered to be more active for catalytic applications. Hence, our finding from simulations that the Pt and Mo atoms form pairs along the edge of Pt-Mo nanoparticles should be an important result for designers of Pt-Mo catalysts.

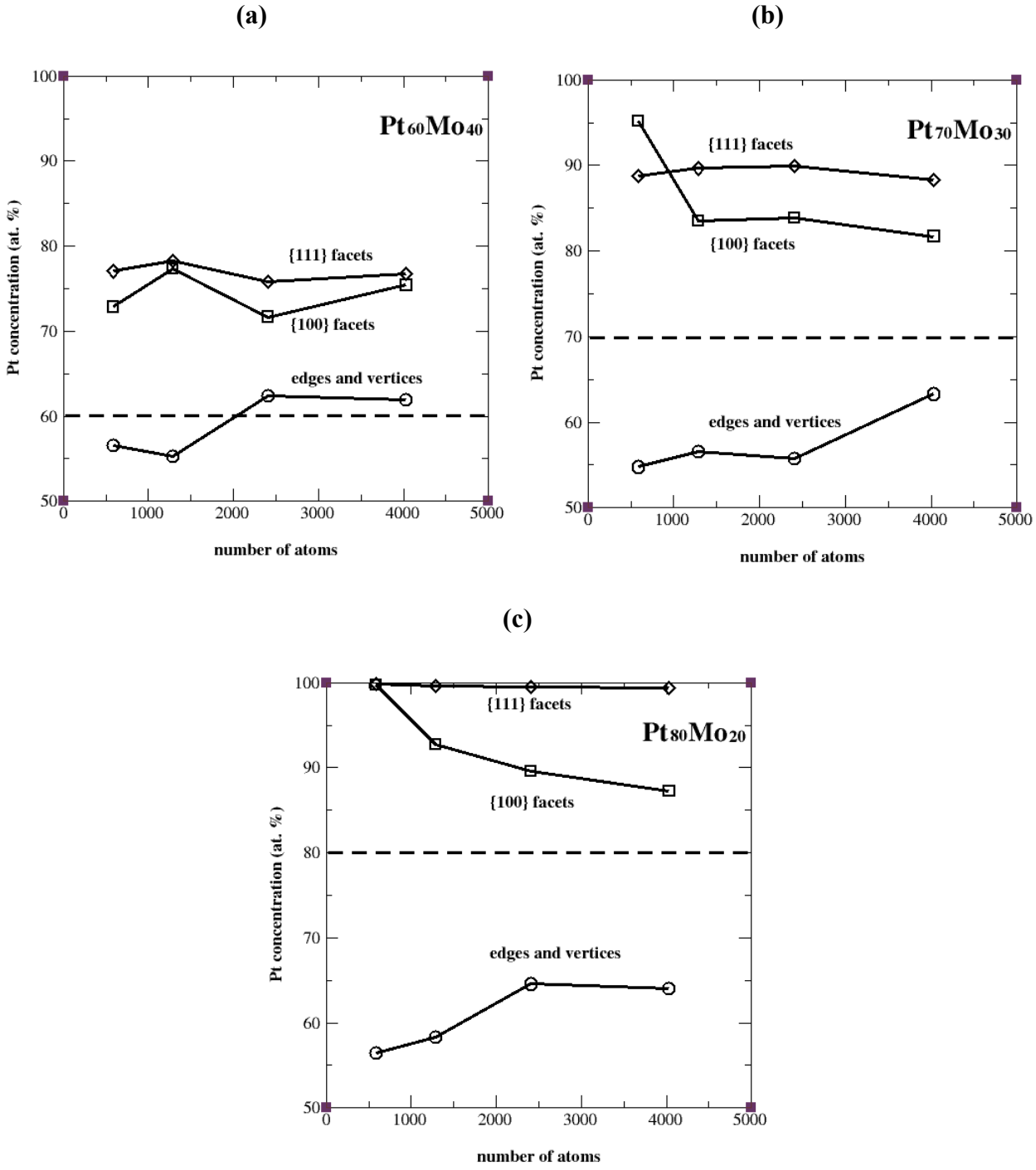

Figure 6. Calculated atomic concentration of Pt atoms at various surface sites as a function of the number of atoms in Pt-Mo nanoparticles at T=600 K. (a) $Pt_{60}Mo_{40}$ nanoparticles, (b) $Pt_{70}Mo_{30}$ nanoparticles, and (c) $Pt_{80}Mo_{20}$ nanoparticles. In the panels, the diamonds represent the results of {111} facets, the squares represent the results of {100} facets, and the circles represent the results of low-coordination edge and vertex sites. The dashed lines indicate the overall Pt concentration in the nanoparticles.

Coordination number of atoms. Extended X-ray absorption fine structure (EXAFS) can be used to determine the atomic number, neighbor distances and coordination number of the element whose absorption edge is being examined, by measuring the backscattering photoelectrons with energies above the absorption edge of a component element in nanoparticles. [38] Thus, EXAFS is one of the most powerful characterization methods for obtaining the detailed structure of nanoparticles. [39] For example, it is from EXAFS data that the core-shell structures of Pt-Pd [40] and Pt-Ru [41] nanoparticles were deduced. To enable comparison of our MC simulations with future EXAFS results, we calculate and show in Table 6 the average coordination numbers of the Pt and Mo atoms in the Pt-Mo nanoparticles equilibrated at 600 K. All results in Table 6, except for the $Pt_{80}Mo_{20}$ nanoparticle with 586 atoms, show that the Mo atoms have more first nearest neighbors than the Pt atoms. Because the bulk atoms have more nearest neighbors than the surface atoms, a core-shell structure (Pt-enriched surface and Mo-enriched core) can be inferred from these data for Pt-Mo nanoparticles. The coordination numbers of the Pt and Mo atoms in Table 6 only differ by a small amount. This implies that the Pt atoms only slightly segregate to the nanoparticle surface, consistent with our results in Fig. 5.

The arrangement of the two metals at the surface of Pt-Mo nanoparticles is more relevant to their application as catalysts than inside the nanoparticles. By reflecting X-rays from a surface at grazing incidence and detecting the resultant X-ray fluorescence, a more surface sensitive technique (known as ReflEXAFS [42]) can be used to determine the coordination number of surface atoms (at least for extended surfaces). To shed light on the preferential segregation of the atoms in the surfaces of Pt-Mo nanoparticles with this type of results, we report in Table 7 the average coordination numbers of the Pt

and Mo atoms at the outermost layer of the Pt-Mo nanoparticles. It is found that the Mo atoms have fewer first nearest neighbors than the Pt atoms at the surface of Pt-Mo nanoparticles. As revealed in Fig. 6, this is because the Mo atoms mostly occupy the low-coordination surface sites such as edges and vertices while the Pt atoms preferentially segregate to the facets. Moreover, the coordination number difference between the Pt and Mo atoms in the surface increases with increasing Pt concentration. This trend can be explained as follows (see Fig. 6): the Pt concentration within facets (with more nearest neighbors) increases with the overall Pt concentration of the Pt-Mo nanoparticles, but not at low-coordination sites. In the $Pt_{80}Mo_{20}$ nanoparticle containing 586 atoms, the Mo atoms in the surface on average have 6.8 first-nearest neighbors and the Pt concentration in the surface is only 4.5 at. % higher than the overall Pt concentration. This leads to the result (see Table 6) that the Pt atoms have a larger coordination number than the Mo atoms in this nanoparticle. It should be noted that the $Pt_{80}Mo_{20}$ nanoparticles containing 586 atoms also have a Pt-enriched surface and a Mo-enriched core (shown in Figs. 3 and 5), instead of a randomly distributed structure or a Mo-enriched surface and Pt-enriched core structure.

EXAFS has been applied to Pt-Mo catalysts. [43-45] However, a direct comparison between theory and experiment requires a more rigorous characterization of the shape, size, composition, and surface morphology of the experimentally prepared nanoparticles. Our current MC simulations only generate equilibrium cubo-octahedral Pt-Mo nanoparticles with complete shells. In contrast, the real Pt-Mo nanoparticles may contain incomplete shells and have different shapes. Therefore, our simulation results in Tables 6 and 7 can serve as references for comparison with EXAFS data in order to evaluate whether the prepared Pt-Mo catalysts assume their equilibrium cubo-octahedral structures.

Mixing of Pt and Mo. To enhance the catalytic performance of Pt by a second element, a good mixing of the two metals in the nanoparticle surfaces is important: Pt and Mo atoms should bond to each other. To illustrate the degree of such Pt-Mo bonding in the outermost layer of Pt-Mo nanoparticles, we calculated the two fractions $F_{Pt\text{-}Mo}$ and $F_{Mo\text{-}Mo}$ in Table 8: $F_{Pt\text{-}Mo}$ (=1-$F_{Pt\text{-}Pt}$) is the averaged fraction of nearest-neighbor atoms to a Pt surface atom that are Mo atoms; $F_{Mo\text{-}Mo}$ (=1-$F_{Mo\text{-}Pt}$)

is the averaged fraction of nearest-neighbor atoms to a Mo surface atom that are Mo atoms. Thus, we look for a large F_{Pt-Mo} and a small F_{Mo-Mo} for well-mixed Pt-Mo nanoparticles. These results should be also measurable using EXAFS or ReflEXAFS.

The results in Table 8 indicate a good mixing tendency for the Pt and Mo atoms in Pt-Mo nanoparticles. For the Pt surface atoms, a high fraction (comparable to the Mo concentration in the nanoparticles) of its nearest neighbors are Mo atoms. DFT calculations [20,46] suggest that the existence of Mo near Pt would modify the electronic structure of the Pt atoms and enhance their catalytic behavior. Therefore, our results indicate that varying the composition of Pt-Mo nanoparticles is a way to control the number of Mo atoms around Pt surface atoms and hence tailor the catalytic properties of these Pt atoms. In Pt-Mo catalysts, the Mo-Mo pairs are not desirable since Mo does not have favorable catalytic properties by itself. Our results in Table 8 show that the Mo surface atoms have fewer Mo first-neighbors than the overall Mo concentration in the nanoparticles. In $Pt_{80}Mo_{20}$ nanoparticles, nearly all the Mo surface atoms have only Pt atoms as nearest neighbors.

Discussion. To design Pt-Mo catalysts at the nanoscale for fuel cells, we consider two properties of the nanoparticle surfaces as a function of their size and composition: Pt concentration and number of Pt-Mo pairs. In real applications, the performance of catalysts is evaluated relative to the total weight of the materials. Therefore, we multiply these two surface properties by the dispersion (also called surface/volume ratio) given in Table 5 of the nanoparticles. In this way, the smaller nanoparticles would tend to be more economical due to their larger dispersions. Figure 7 plots our results obtained from the MC simulations at T=600 K. Note that, according to Fig. 7(a), the Pt concentration in nanoparticle surfaces increases with decreasing nanoparticle size. Although the Pt concentrations in the surfaces of small nanoparticles are intrinsically lower, as shown in Fig. 5, the smaller nanoparticles have a larger dispersion and thus expose relatively more Pt atoms to reactants than do larger nanoparticles.

For the application of Pt-Mo catalysts in fuel cells, Pt is the only active metal. Hence, the more Pt atoms that are in the surfaces, the better catalytic performance the Pt-Mo nanoparticles would have. Our results in Fig. 7(a) for Pt-Mo nanoparticles indicate that both decreasing nanoparticle size and

increasing overall Pt concentration in nanoparticles lead to higher Pt concentrations in the nanoparticle surfaces. On the other hand, the Pt and Mo atoms should bond to each other in the surface of Pt-Mo catalysts to tolerate CO. We counted the Pt-Mo pairs in the equilibrium Pt-Mo nanoparticle surfaces and plotted the results in Fig. 7(b). Figure 7(b) shows that both increasing nanoparticle size and decreasing overall Pt concentration in nanoparticles leads to more Pt-Mo pairs in the nanoparticle surfaces. For $Pt_{60}Mo_{40}$ nanoparticles, the change of nanoparticle size has a dramatic effect on the number of Pt-Mo pairs in the nanoparticle surfaces. In contrast, the change of nanoparticle size has little effect on the number of Pt-Mo pairs in the surfaces of $Pt_{80}Mo_{20}$ nanoparticles. For cubo-octahedral nanoparticles, the total number of atoms at the edges and vertices (see Table 5) increases only slightly with nanoparticle size ($N^{1/3}$). Since the Mo atoms mostly appear at the low-coordination surface sites and the Pt and Mo atoms alternate along the edges and vertices in $Pt_{80}Mo_{20}$ nanoparticles (see Fig. 3(c)), the number of Pt-Mo pairs would increase only slightly with nanoparticle size as shown in Fig. 7(b).

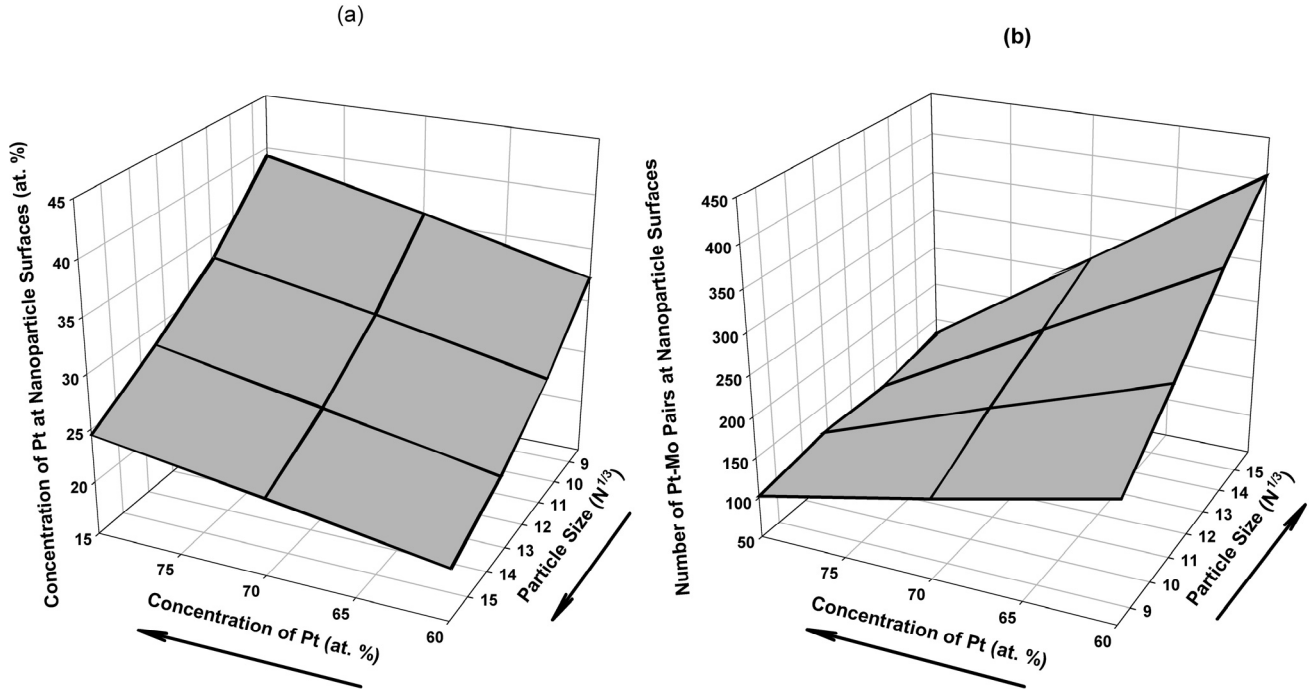

Figure 7. Calculated Pt concentration (a) and number of Pt-Mo pairs (b), after multiplication by the dispersion, in nanoparticle surfaces as a function of the size ($N^{1/3}$, proportional to radius) and composition of Pt-Mo nanoparticles. N is the total number of atoms in the nanoparticles. The size axis is reversed in (a) for better display of the data.

In Pt-Mo alloy surfaces, a high Pt concentration would enhance the activity of H_2 oxidation reactions, while a larger number of Pt-Mo pairs (hence decreasing Pt concentration) would enhance the CO tolerance. As a result, it was found experimentally that the $Pt_{77}Mo_{23}$ surface is more active for the oxidation of a H_2/CO mixture than either $Pt_{67}Mo_{33}$ or $Pt_{85}Mo_{15}$ surfaces. [17] Our simulation results in Fig. 7 indicate that two surface properties (Pt concentration and number of Pt-Mo pairs) will change in opposite directions when varying the size and composition of Pt-Mo nanoparticles. This may suggest that there exists an optimal size and composition for Pt-Mo nanoparticles to yield the best catalytic performance in the electro-oxidation of H_2/CO mixtures.

Conclusions

We have investigated the surface structures of the equilibrium fcc cubo-octahedral Pt-Mo catalyst nanoparticles at the atomistic scale, using MEAM potentials and the Monte Carlo method. The MEAM potentials that we developed can reproduce most of the available data for the pure Pt metal that assumes an fcc crystal lattice, the pure Mo metal that adopts a bcc structure, and the intermetallic compound Pt_3Mo, which has a $L1_2$ structure. From our MC simulations at T=1000 K, we predict a weak segregation of Pt atoms to the relaxed low-index extended surfaces of Pt-Mo alloys. The theoretical results agree well with the experimental measurement of Pt-Mo polycrystal surfaces. [13] Therefore, our MEAM potentials and the Monte Carlo method are suitable for studying the equilibrium Pt-Mo nanoparticle surface structure, which is a result of the preferential segregation of Pt atoms to various surface sites.

In this work, we assume the fcc cubo-octahedron with complete shells as the equilibrium shape of Pt-Mo nanoparticles. To investigate the influence of both size and composition on the equilibrium Pt-Mo nanoparticle structures, we constructed cubo-octahedral nanoparticles containing 586, 1289, 2406, and 4033 atoms (corresponding to a particle diameter from 2.5 to 5 nm) and with compositions of 60, 70, 80, and 90 at. % of Pt. We found that a {100} facet can reconstruct from a bulk terminated square lattice to a hexagonal arrangement of atoms, but only in Pt-rich nanoparticles (such as $Pt_{90}Mo_{10}$) when the facet is completely free of Mo atoms.

We performed detailed analyses for the surface structures of the $Pt_{60}Mo_{40}$, $Pt_{70}Mo_{30}$, and $Pt_{80}Mo_{20}$ nanoparticles. The Pt concentrations in the surfaces are predicted to be 5 to 14 at. % higher than the overall Pt concentration of these nanoparticles. Hence, the equilibrium Pt-Mo nanoparticle has a core-shell structure with a slightly Pt-enriched shell and a slightly Pt-deficient core. We show in this work that the core-shell structures of Pt-Mo nanoparticles should be observable by measuring the coordination numbers of the Pt and Mo atoms using the EXAFS technique. Moreover, we found that the Pt atoms segregate most prominently to the {111} and {100} facets in nanoparticle surfaces. Regardless of their compositions, the simulated Pt-Mo nanoparticles with the same size have nearly the same Pt concentrations at the low-coordination sites (including edges and vertices). The Pt and Mo atoms tend to alternate along these low-coordination surface sites.

Our results indicate that the Pt and Mo atoms mix well, pairing up in Pt-Mo nanoparticles. More importantly, we found for Pt surface atoms that the fraction of Mo atoms in their nearest neighbors is close to the overall Mo concentration in the nanoparticles. This suggests a way to tailor the catalytic performance of Pt with Mo by varying the nanoparticle composition. In general, we found that decreasing the size or increasing the overall Pt concentration leads to higher Pt concentrations but fewer Pt-Mo pairs in the nanoparticle surfaces. This implies that there exist an optimal size and composition for Pt-Mo nanoparticles to achieve the best catalytic performance in the electro-oxidation of H_2/CO mixtures. Hence, our study of the surface structures of cubo-octahedral Pt-Mo nanoparticles should be useful for future processing, characterization, improvement, and design of Pt-Mo nanoparticles as electro-catalysts in fuel cells.

Acknowledgment. This work was supported by the Office of Science, Materials Sciences Division, of the U.S. Department of Energy under Contract Nos. DE-AC03-76SF00098 at LBNL and W-7405-ENG-36 at LANL. The computations were carried out at the National Energy Research Scientific Computing Center (NERSC), which is operated by LBNL for the U.S. Department of Energy.

TABLES

Table 1: MEAM potentials parameters for Mo, Pt and Pt_3Mo. The parameters are: the cohesive energy E_c (eV), the equilibrium nearest-neighbor distance r_e (Å), the exponential decay factor for the universal energy function α, the scaling factor for the embedding energy A, the four exponential decay factors for the atomic densities $\beta^{(i)}$, the four weighting factors for the atomic densities $t^{(i)}$, and the density scaling factor ρ_0. See Refs. 10 and 11 for the detailed definitions of these parameters.

	E_c	r_e	α	A	$\beta^{(0)}$	$\beta^{(1)}$	$\beta^{(2)}$	$\beta^{(3)}$	$t^{(0)}$	$t^{(1)}$	$t^{(2)}$	$t^{(3)}$	ρ_0
Mo	6.81	2.73	5.85	0.58	8.00	8.00	8.00	1.00	1.00	3.00	5.10	-3.00	1.60
Pt	5.77	2.77	6.44	1.04	4.673	2.20	6.00	2.20	1.00	4.70	-1.38	3.29	1.00
Pt-Mo	6.123	2.756	6.64	-	-	-	-	-	-	-	-	-	-

Table 2: Angular screening parameters for the MEAM potentials for Pt-Mo. See Ref. 11 for the details for the screening function.

	Pt-Pt-Pt	Pt-Mo-Pt	Mo-Pt-Pt	Mo-Mo-Pt	Mo-Pt-Mo	Mo-Mo-Mo
C_{max}	2.8	1.0	2.8	2.8	2.8	2.8
C_{min}	2.0	0.0	2.0	2.0	2.0	0.5

Table 3: Comparison of the calculated properties of bulk Pt_3Mo ($L1_2$) using the MEAM potentials and the first-principles calculation method. The cohesive energies are given relative to the energies of the fcc Pt and bcc Mo. These properties are used to fit the cross potential between Pt and Mo.

	MEAM	First-principles method
Lattice constant a (Å)	3.898	3.897
Cohesive energy (eV/atom)	-0.093	-0.093
Elastic constant B (GPa)	324.5	324.1
Elastic constant $C_s = (C_{11}-C_{22})/2$ (GPa)	36.5	71.4
Elastic constant C_{44} (GPa)	77.7	150.8

Table 4: Energies of the relaxed extended low-index surfaces for bcc Mo and fcc Pt calculated using the MEAM potentials, compared to first-principles and experimental results. The surface energies are in unit of mJ/m^2. The equilibrium lattice constant is 3.15 Å for bcc Mo and 3.92 Å for fcc Pt.

	surfaces	MEAM	First-principles [a]	Experiment
Mo (bcc)	(111)	3116	3740	2907 [b], 3000 [c]
	(100)	3144	3837	
	(110)	2932	3454	
Pt (fcc)	(111)	1651	2299	2489 [b], 2475 [c]
	(100)	2154	2734	
	(110)	1963	2819	

[a] Reference 28.

[b] Reference 29.

[c] Reference 30.

Table 5: Total number of atoms and number of atoms at various surface sites in the cubo-octahedral nanoparticles with complete shells. These nanoparticles can be represented by m, m being the number of atoms on an edge. The table also includes the calculated dispersion, which is the number of atoms at the surfaces divided by the total number of atoms of the particles (including the surfaces).

	m=4	m=5	m=6	m=7
Total	586	1289	2406	4033
Vertex	24	24	24	24
{111}/{111} edges	24	36	48	60
{111}/{100} edges	48	72	96	120
{100} facets	24	54	96	150
{111} facets	152	296	488	728
Dispersion	0.464	0.374	0.313	0.268

Table 6: Coordination numbers of the Pt and Mo atoms in Pt-Mo nanoparticles determined by Monte Carlo simulations at 600 K. For comparison, we include the coordination number of the atoms in a nanoparticle with randomly distributed Pt and Mo (no segregation). For a detailed comparison with future EXAFS data, we also include the calculated partial coordination numbers for atoms in parentheses. The two numbers in parentheses for Pt atoms are the partial coordination numbers of Pt-Pt and Pt-Mo pairs, respectively. The two numbers in parentheses for Mo atoms are the partial coordination numbers of Mo-Pt and Mo-Mo pairs, respectively. N is the number of atoms in the nanoparticles.

	N=586	N=1289	N=2406	N=4033
$Pt_{60}Mo_{40}$				
Pt	10.0 (5.4; 4.6)	10.4 (5.6; 4.8)	10.6 (5.6; 5.0)	10.8 (5.7; 5.1)
Mo	10.5 (6.9; 3.6)	10.9 (7.2; 3.7)	11.1 (7.5; 3.6)	11.4 (7.7; 3.7)
$Pt_{70}Mo_{30}$				
Pt	10.1 (6.5; 3.6)	10.5 (6.8; 3.7)	10.7 (6.9; 3.8)	10.9 (7.0; 3.9)
Mo	10.4 (8.3; 2.1)	10.9 (8.7; 2.2)	11.2 (8.9; 2.3)	11.4 (9.1; 2.3)
$Pt_{80}Mo_{20}$				
Pt	10.2 (7.9; 2.3)	10.5 (8.1; 2.4)	10.7 (8.2; 2.5)	11.0 (8.4; 2.6)
Mo	10.1 (9.3; 0.8)	10.8 (9.7; 1.1)	11.3 (10.2; 1.1)	11.5 (10.3; 1.2)
Random (Pt or Mo)	10.2	10.6	10.9	11.1

Table 7: As Table 6, but only for atoms in the outermost layer of Pt-Mo nanoparticles.

	N=586	N=1289	N=2406	N=4033
$Pt_{60}Mo_{40}$				
Pt	8.2	8.4	8.5	8.5
Mo	7.8	8.0	8.2	8.3
$Pt_{70}Mo_{30}$				
Pt	8.3	8.4	8.5	8.6
Mo	7.4	7.7	7.8	8.0
$Pt_{80}Mo_{20}$				
Pt	8.4	8.5	8.5	8.6
Mo	6.8	6.9	7.1	7.1
Random (Pt or Mo)	8.1	8.3	8.4	8.5

Table 8: Degree of mixing between Pt and Mo atoms in the surface of Pt-Mo nanoparticles determined by MC simulations at 600 K. See definitions of F_{Pt-Mo} and F_{Mo-Mo} in the text. N is the number of atoms in the nanoparticles. C_{Mo} is the fraction of Mo atoms in the whole nanoparticle.

	N=586	N=1289	N=2406	N=4033
$Pt_{60}Mo_{40}$ (C_{Mo}=0.40)				
F_{Pt-Mo}	0.40	0.38	0.38	0.36
F_{Mo-Mo}	0.15	0.14	0.13	0.12
$Pt_{70}Mo_{30}$ (C_{Mo}=0.30)				
F_{Pt-Mo}	0.29	0.26	0.24	0.23
F_{Mo-Mo}	0.07	0.06	0.05	0.05
$Pt_{80}Mo_{20}$ (C_{Mo}=0.20)				
F_{Pt-Mo}	0.17	0.14	0.12	0.10
F_{Mo-Mo}	0.01	0.01	0.01	0.00

REFERENCES

(1) *Basic Research Needs for the Hydrogen Economy*, report of the basic energy sciences workshop on hydrogen production, storage, and use (March, 2003). Available on the web at http://www.sc.doe.gov/bes/hydrogen.pdf.

(2) Markovic, N. M.; Ross, P. N. *Surf. Sci. Rep.* **2002**, 45, 117.

(3) Toda, T.; Igarashi, H; Uchida, H.; Watanabe, M. *J. Electrochem. Soc.* **1999**, 146, 3750.

(4) Paulus, U. A.; Wokaun, A.; Scherer, G. G.; Schmidt, T. J.; Stamenkovic, V.; Radmilovic, V.; Markovic, N. M.; Ross, P. N. *J. Phys. Chem. B* **2002**, 106, 4181.

(5) Antolini, E.; Passos, R. R.; Ticianelli, E. A. *Electrochim. Acta* **2002**, 48, 263.

(6) Sasaki, K.; Mo, Y.; Wang, J. X.; Balasubramanian, M.; Ubribe, F.; McBreen, J.; Adzic, R. R. *Electrochim. Acta* **2003**, 48, 3841.

(7) Strohl, J. K.; King, T. S. *J. Catal.* **1989**, 116, 540.

(8) Mainardi, D. S.; Baluena, P. B. *Langmuir* **2001**, 17, 2047.

(9) Molenbroek, A. M.; Norskov, J. K.; Clausen, B. S. *J. Phys. Chem. B* **2001**, 105, 5450.

(10) Baskes, M. I. *Phys. Rev. B* **1992**, 46, 2727.

(11) Wang, G.; Van Hove, M. A.; Ross, P. N.; Baskes, M. I. *J. Chem. Phys.* **2004**, 121, 5410.

(12) Wang, G.; Van Hove, M. A.; Ross, P. N.; Baskes, M. I. *J. Chem. Phys.* **2005**, 122, 024706.

(13) Grgur, B. N.; Markovic, N. M.; Ross, P. N. *J. Phys. Chem. B* **1998**, 102, 2494.

(14) Daw, M.S.; Baskes, M.I. *Phys. Rev. Lett.* **1983**, 50, 1285.

(15) Daw, M.S.; Baskes, M.I. *Phys. Rev. B* **1984**, 29, 6443.

(16) Grgur, B. N.; Zhuang, G.; Markovic, N. M.; Ross, P. N. *J. Phys. Chem. B* **1997**, 101, 3910.

(17) Grgur, B. N.; Markovic, N. M.; Ross, P. N. *J. Electrochem. Soc.* **1999**, 146, 1613.

(18) Santiago, E. I.; Camara, G. A.; Ticianelli, E. A. *Electrochim. Acta* **2003**, 48, 3527.

(19) Mukerjee, S.; Urian, R. C.; Lee, S. J.; Ticianelli, E. A.; McBreen, J. *J. Electrochem. Soc.* **2004**,151, A1094.

(20) Shubina, T. E.; Koper, M. T. M. *Electrochim. Acta* **2002**, 47, 3621.

(21) Lee, B.J.; Baskes, M.I. *Phys. Rev. B* **2000**, 62, 8564.

(22) Lee, B.J.; Baskes, M.I.; Kim, H.; Cho, Y.K. *Phys. Rev. B* **2001**, 64, 184102.

(23) Baskes, M.I.; Angelo, J.E.; Bisson, C.L. *Modell. Simul. Mater. Sci. Eng.* **1994**, 2, 505.

(24) Pfrommer, B. G.; Coté, M.; Louie, S. G.; Cohen, M. L. *J. Comp. Phys.* **1997**, 131, 233.

(25) Pfrommer, B. G.; Demmel, J.; Simon, H. *J. Comp. Phys.* **1999**, 150, 287.

(26) Fuchs, M.; Scheffler, M. *Comput. Phys. Commun.* **1999**, 119, 67.

(27) Troullier, N.; Martins, J. L. *Phys. Rev. B* **1991**, 43, 1993.

(28) Vitos, L.; Ruban, A. V.; Skriver, H. L.; Kollár, *J. Surf. Sci.* **1998**, 411, 186.

(29) Tyson W. R.; Miller, W. A. *Surf. Sci.* **1977**, 62, 267.

(30) De Boer, F. R.; Room, R.; Mattens, W. C.; Miedama, A. R.; Niessen A. K. *Cohesion in Metals*; North-Holland: Amsterdam, 1988.

(31) Saunders, N.; Miodownik, A. P.; Dinsdale, A. T. *CALPHAD* **1988**, 12, 351.

(32) Raub, E. *Z. Metallk.* **1954**, 45, 23.

(33) Mukherjee, S.; Morán-López, J. L. *Surf. Sci.* **1987**, 188, L742.

(34) Frenkel, A. I.; Hills, C. W.; Nuzzo, R. G. *J. Phys. Chem. B* **2001**, 105, 12689.

(35) Van Hardeveld, R.; Hartog, F. *Surf. Sci.* **1969**, 15, 189.

(36) Van Hove, M. A.; Koestner, R. J.; Stair, P. C.; Bibérian, J. P.; Kesmodel, L. L.; Bartoš, I.; Somorjai, G. A. *Surf. Sci.* **1981**, 103, 189.

(37) Van Hove, M. A.; Koestner, R. J.; Stair, P. C.; Bibérian, J. P.; Kesmodel, L. L.; Bartoš, I.; Somorjai, G. A. *Surf. Sci.* **1981**, 103, 218.

(38) Stern, E. A.; Heald, S. M. In *Handbook of Synchrotron Radiation*; Koch, E. E. Ed.; North-Holland: Amsterdam, 1983; Chapter 10.

(39) Toshima, N.; Yonezawa, T *New J. Chem.* **1998**, 22, 1179.

(40) Kolb, U; Quaiser, S. A.; Winter, M.; Reetz, M. T. *Chem. Mater.* **1996**, 8, 1889.

(41) Nashner, M. S.; Frenkel, A. I.; Somerville, D.; Hills, C. W.; Shapley, J. R.; Nuzzo, R. G. *J. Am. Chem. Soc.* **1998**, 120, 8093.

(42) Greaves, G. N. *Adv. X-ray Analysis* **1991**, 34, 13.

(43) Samant, M. G.; Bergeret, G.; Meitzner, G.; Gallezot, P.; Boudart, M. *J. Phys. Chem.* **1988**, 92, 3547.

(44) Choi, S. H.; Lee, J. S. *J. Catal.* **1997**, 167, 364.

(45) Mukerjee, S.; Urian, R. C. *Electrochim. Acta* **2002**, 47, 3219.

(46) Ishikawa, Y.; Liao, M. S.; Cabrera, C. R. *Surf. Sci.* **2002**, 513, 98.